



An examination of microwave rainfall retrieval biases and their characteristics over the Amazon

Izabelly C. Costa^{a,*}, Luiz A.T. Machado^a, Christian Kummerow^b

^a National Institute for Space Research – INPE, Center for Weather Forecast and Climate Studies – CPTEC, Rodovia Presidente Dutra, km 40, Cachoeira Paulista, São Paulo, Brazil

^b Department of Atmospheric Science, Colorado State University, Fort Collins, CO, United States



ARTICLE INFO

Keywords:

Satellite rainfall estimation
Passive microwave rainfall estimation
Satellite rainfall estimation errors

ABSTRACT

Estimates of surface precipitation obtained from passive microwave sensors over land are closely related to the ice path present in the clouds. However, there are cloud types without any ice or with an ice layer not thick enough to justify the associated rainfall. For these cloud types, the precipitation is not estimated correctly, causing an underestimation of the precipitation. On the other hand, there are cases of deep clouds, in which the signal produced by ice scattering is not effectively associated with precipitation, producing, in turn, an overestimate of rainfall. This study analyzes cases that have large errors in the rainfall estimates obtained from passive microwave data to better understand and potentially mitigate these biases. This study uses data from the Tropical Rainfall Measuring Mission (TRMM) satellite, specifically the Precipitation Radar (PR), TRMM Microwave Imager (TMI) and Lightning Imaging Sensor (LIS). Ten years of TRMM data (2002–2011) are used in the analysis. The study area is approximately 1,110,000 km², centered on the city of Manaus in the Amazon region. The error distribution resembled a Gaussian distribution. The error population was then divided into three categories, one class denominated as consistent, in the center of the distribution (20 percentile to 80 percentile), and the others two, as under- and over-estimated populations, representing the tails of the distribution. For under- and over-estimated categories, the vertical structure of the clouds was evaluated. The underestimation error is correlated with almost all cloud properties (rain rate, cloud top, Liquid Water path (LWP), Ice Water Path (IWP), polarization and Polarization Corrected Temperature at 85 GHz (PCT85)) while the overestimation error is only function of the IWP. The use of combinations of low and high frequency channels was able to identify some characteristics associated with under- and over-estimated cases. A high positive difference between the 10 GHz and 85 GHz as well as 19 GHz – 85 GHz is characteristic of very high scattering at 85 GHz (high amount of ice) and small liquid water amounts corresponding to cases that are often overestimated by the radiometer. On the other hand, underestimated cases have smaller ice particles that are not sensitive to the high frequency microwaves channels measured by TMI. These results open potential new avenues to improve the quality of passive microwave rainfall estimates.

1. Introduction

Satellite borne radiometers operating in the passive microwave frequency range measure the radiation emitted and scattered by the surface, atmospheric gases and the solid and liquid phases of water. Based on the interactions between the atmospheric hydrometeors and the microwave radiation, two processes can be used to estimate precipitation: emission/absorption from raindrops, which causes brightness temperature to increase over a radiatively cold background like the ocean and the scattering by the larger hydrometeors, which causes a decrease in microwave radiation (Kidd and Levizzani, 2011; Prigent

et al., 2005).

Precipitation estimation from passive microwave over oceans is well established, as the low surface emissivity allows for a strong contrast between a radiometrically cold background and a warm precipitation-related atmospheric signature (Kummerow et al., 2001, 2011). Rainfall retrieval over land, however, remains problematic (Carr et al., 2015), because of the higher and variable surface emissivity which appears very similar to the emission from clouds and precipitation. High-frequency channels are therefore more frequently used to estimate rainfall over land (Gopalan et al., 2010), based primarily on brightness temperature depression caused by ice scattering, coupled to some

* Corresponding author.

E-mail address: izabelly.costa@inpe.br (I.C. Costa).

relationship between the ice aloft and the surface rain rate.

The ice water content and particle habits may be used as an indicator of its precipitation potential. The ice water content of a system can also be related to electrical activity. The work of [Mattos and Machado \(2011\)](#) suggested that an increase in the average occurrence of cloud to ground lightning is associated with an increment in ice particle size and ice water content. [Petersen et al. \(2005\)](#) used lightning and radar observations of TRMM to study the fundamental relationship between precipitation ice mass and lightning flash density. The results indicated that, on a global scale, the relationship between precipitation ice water path and lightning flash density is relatively invariant between land, ocean and coastal regimes. These indicators can be applied to passive microwave-based rainfall estimation algorithms over land ([Ferraro et al., 2005](#); [Vila et al., 2007](#); [Weng et al., 2003](#)). However, there are cloud types without ice layers or with an ice layer not thick enough to justify the associated rainfall. Such clouds are common in the Amazon during the wet season, when the Cloud Condensation Nuclei (CCN) concentrations are relatively small while the humidity is high. As a result, clouds droplets rapidly grow to rain drops and fall without going through an ice process. These clouds do not have much time to grow, reaching a maximum height of 4 or 5 km ([Silva Dias et al., 2005](#)). According to [Nesbitt et al. \(2000\)](#) the occurrence of precipitation features without an ice scattering signature is often observed in the Tropical region and is poorly quantified using an ice scattering techniques alone.

On the other hand, there are also cases of deep clouds where ice scattering signature inferred by satellites are not well correlated with rainfall. These cloud types will be problematic for satellite based precipitation schemes as well. According to [You et al. \(2011\)](#), the frozen hydrometeor population aloft often has an inconsistent and less direct relation with surface rainfall and varies significantly from region to region.

The diversity of the precipitating cloud systems makes the understanding of the vertical structure of storm systems a subject of great importance for satellite rainfall estimation over land. The main goal of this study is to evaluate the radiative properties, the vertical structure, and the broader characteristics of the clouds in which cloud ice water content lacks a direct relationship to precipitation. The knowledge of the physical behavior of these clouds provides the basis for further refinements in microwave rainfall estimation algorithms.

[Section 2](#) describes the satellite data used in this work. [Section 3](#) describes the classification strategy employed to identify clouds that either overestimate or underestimate rainfall. [Section 4](#) presents the cloud vertical structure for these overestimated and underestimated cloud types, while [Section 5](#) evaluates the potential of lower channels frequencies to identify characteristics of the overestimated and underestimated cases. Finally, conclusions are presented in [Section 6](#).

2. Data

This study uses data from the Tropical Rainfall Measuring Mission (TRMM) satellite, made available by the University of Utah. The data is produced with a combination of the version 7 orbital 1B01, 1B11, 2A12 ([Kummerow et al., 2001](#)), 2A23, 2A25 ([Iguchi et al., 2000](#)), 2B31, 2H25 and version 4 of the LIS granules after TMI-PR (TRMM Microwave Imager - Precipitation Radar) parallax correction and TMI-PR-LIS-VIRS (Lightning Imaging Sensor - Visible and Infrared Scanner) nearest neighbor co-location ([Liu, 2013](#)). Ten years of TRMM data are used (2002–2011) for the current analysis. In order to avoid data with different spatial resolutions, only data after the orbit boost maneuver in August 2001 are used. To avoid possible inconsistencies associated with pixel collocation, the TMI-PR paired search was done using a matrix of 3×3 PR pixels for each TMI pixel (similar to [Kidd et al., 2017](#)), selecting the PR value with the smallest difference in rain rate when compared to the TMI precipitation using the Goddard Profiling Algorithm (GPROF – [Kummerow et al., 1996](#)).

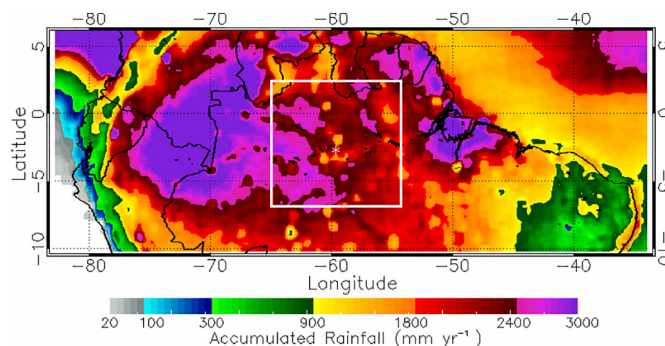


Fig. 1. Studied region indicated by the white box and the mean annual rainfall for the period from 2002 to 2010 using the MERGE data.

An area of the Amazon ([Fig. 1](#)) was chosen due to the frequent occurrence of deep and shallow convective clouds ([Giangrande et al., 2017](#)). According to the MERGE data product ([Rozante et al., 2010](#)), a technique that combines TRMM satellite precipitation estimates with surface observations over South America, mean annual rainfall in the study region varies from 1450 to 3000 mm.

We used the vertical profiles of reflectivity, surface rain and rain type from PR and lightning information from LIS to define clouds. The 10, 19, 21, 37 and 85 GHz brightness temperatures (T_b) as well as surface rain from the GPROF algorithm were evaluated against the cloud structure information; For the 37 and 85 GHz channels, the polarization corrected brightness temperature (PCT) values are calculated ([Spencer et al., 1989](#)) to reduce the effect of different surface emissivities. Over wet surfaces, the PCT is used to remove radiometrically cold surface features such as a standing water. This correction is pertinent in the Amazon region due to the width of the Amazon River. Only the vertical polarization is used for the other channels. For the lower frequency channels, it was decided to work with the original spatial resolution, as in [You et al. \(2011\)](#). The collocated TMI and PR data were classified according to the rain type data (convective, stratiform and others) available in the PR 2A23 ([Awaka et al., 2009](#)).

The cases classified as convective were subdivided into “convection certain” and “convection possible” as well as “stratiform certain” and “stratiform possible”. This study focuses primarily on the cases classified by the algorithm as “convective certain” in order to focus on these clouds. All other cloud types are groups on the “other” category. The total number of pixels classified by rain type as convective is shown in [Table 1](#).

3. Identification and characterization of the convective cases

In the present study, rainfall from TRMM’s passive microwave sensor (TMI) was estimated using the GPROF algorithm, herein referred as RR_{TMI} . The precipitation radar’s rainfall, herein referred as RR_{PR} , is considered the reference rain rate. While RR_{PR} may have its own error sources, they are generally considered smaller over land than the

Table 1
Statistical errors between GPROF and PR data.

| Statistics for convectives rain | Studied error population |
|---|--------------------------|
| Total pixels | 72,166 |
| Accepted pixels using 50% error criterion | 60,681 |
| Rejected pixels | 11,485 (~16%) |
| Rejected pixels | PR ~ 96% |
| $RR \leq 15 \text{ mm h}^{-1}$ | TMI ~ 78% |
| Mean RR_{PR} | 8.8 mm h^{-1} |
| Mean RR_{TMI} | 8.9 mm h^{-1} |
| RMSE | 2.0 mm h^{-1} |
| Mean error | 15.7% |
| Standard deviation error | 20.1% |

indirect estimates from the radiometer.

As previously mentioned, there are clouds where the amount or the absence of ice aloft does not correspond well to the expected rain rate. These are precisely the cases of interest in the present study, where an overestimate or underestimate of the rain rate is defined based upon RR_{TMI} relative to RR_{PR} . Bias errors are normalized as shown below:

$$Error = \frac{RR_{TMI} - RR_{PR}}{RR_{PR}} \times 100 \quad (1)$$

From the calculated error of each pixel, frequency distributions of these errors were generated as well as the ratio between RR_{TMI} and RR_{PR} versus RR_{PR} (not shown). It was observed that the distribution of ratio between rain rates resembled a Gaussian function, although slightly more elongated for the overestimate errors with a higher frequency of cases with ratio values close to one. In addition, the distribution has a large tail for high bias values, however the higher the RR_{PR} the lower the ratio (error) between precipitation rates. These larger biases are probably associated with co-location errors, particularly since the TMI has a slant path, and the PR is essentially vertically (downward) pointing. This represents a significant amount of scatter when comparing individual pixels, but should not cause systematic biases as the storm and satellite orientations can be thought of as random for the purposes of this study. To eliminate the effect of these outliers, a threshold of -50% to 50% error was defined. Pixels outside this range were eliminated ($\sim 16\%$ – see Table 1). This additional procedure avoids the co-location problems following the same procedure employed by Gopalan et al. (2010).

Fig. 2 shows the error distribution and the under- and overestimated populations. The mean absolute error is 15.7% and the standard deviation is 20.1% . This population is then divided into three categories: A “consistent” class, in the center of the distribution, and the under- and over-estimated classes, representing the tails of the distribution. For this study, the under- and over-estimated classes are defined as the smallest and largest 20 percentile of the distribution respectively, while the consistent class is defined between the 20 and 80 percentile. With this definition, the underestimated class corresponds to errors between -50% and -14.5% , while the overestimated class corresponds to error between $+18.2\%$ and $+50\%$. The consistent class corresponds to errors larger than -14.5% and smaller than 18.2% (Fig. 2). The basic statistics are shown on the Table 1. Although, the 20 percentile limits correspond nearly to the absolute error or the distribution standard

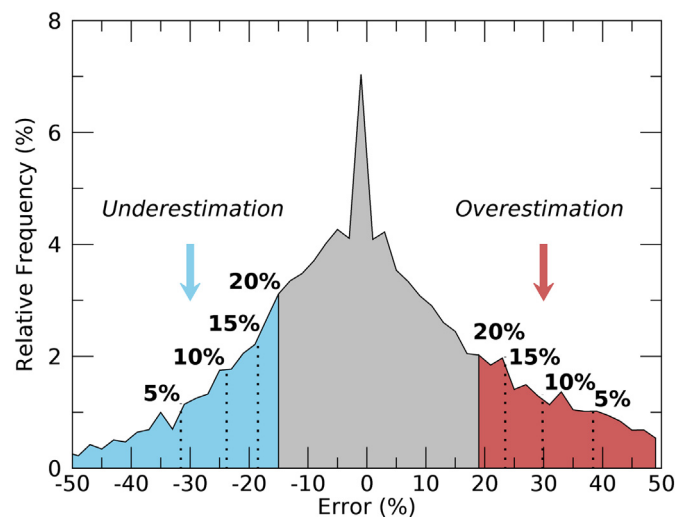


Fig. 2. Frequency distribution of the normalized error calculated using the rain rates estimates from PR and TMI. The colors blue, gray and red represent the three categories, underestimated, consistent and overestimated classes, respectively. (For interpretation of the references to colour in this figure legend, the reader is referred to the web version of this article.)

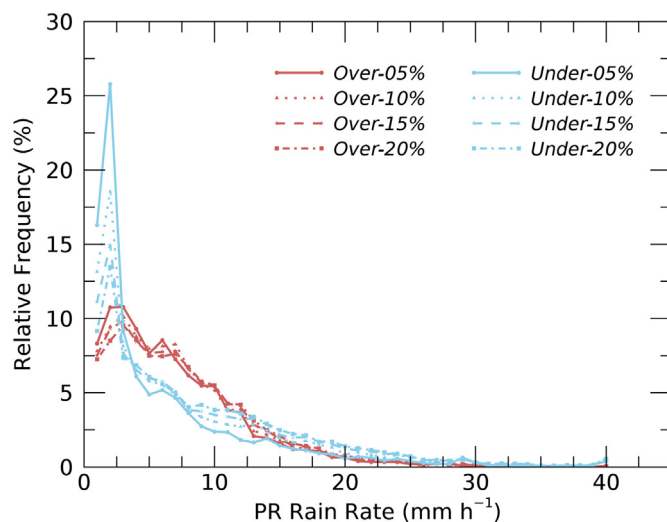


Fig. 3. Underestimated and overestimated cases frequency distribution as function of the rain rates estimates from PR. Under- and over-estimated populations are classified by the 20%, 15%, 10% and 5% percentiles for the tail of the distribution.

deviation, others percentiles were evaluated during the analysis. A 15 percentile limit (-18.5% to 23.5% errors), 10 percentile (-23.8% to 29.8% errors) and 5 percentile (-31.6% to 38.4%) were also considered.

Petković and Kummerow (2017) studied rainfall estimation errors over the Amazon relative to the African Congo region. While the two regions had large overall bias differences, they could attribute the regional biases to systematic differences between PR and TMI rainfall in specific regimes defined in their study as shallow, deep-unorganized, and deep-organized convection. Shallow and deep-unorganized regimes tended to be underestimated by the passive microwave-based algorithm by 33% and 10% , respectively, while, the deep-organized regime rainfall was overestimated by 41% . Regional differences in that study could be accounted for by the difference in the relative frequency of occurrence of each of the cloud regimes. The average error reported in that study are very close to the ones obtained here.

In order to evaluate the relationship between the under- and over-estimated populations as a function of the rain rate, the two distributions were evaluated as a function of the PR rain estimates. Fig. 3 shows the relative frequency distribution determined for the rain rates estimated for the under- and over-estimated populations. Proportionally, underestimated cases have a predominately large populations of relatively small rain rates (smaller than 5 mm h^{-1}), and the errors can be seen to be a function of rain rate. In contrast, overestimated rain rates consist primarily of larger rain rate than the underestimated population, and the absolute error is not a function of the rain rate. There is only a slight difference among the overestimated error among the different percentiles.

4. Cloud vertical structure

The analysis of the vertical structure of the clouds belonging to the under- and over-estimated categories can shed some light on the limitations associated with satellite precipitation estimates from only the passive microwave channels. As hypothesized, the overestimation is related to large ice content, low liquid water content and possibly the bright band presence in the average reflectivity profiles. The opposite occurs in the underestimated cases, where there is probably a thinner ice layer and higher values of liquid water, resulting in an under-estimation of the precipitation rate from the PCT85.

One way to evaluate the cloud vertical structure for each population is to compute the Contoured Frequency by Altitude Diagrams (CFAD).

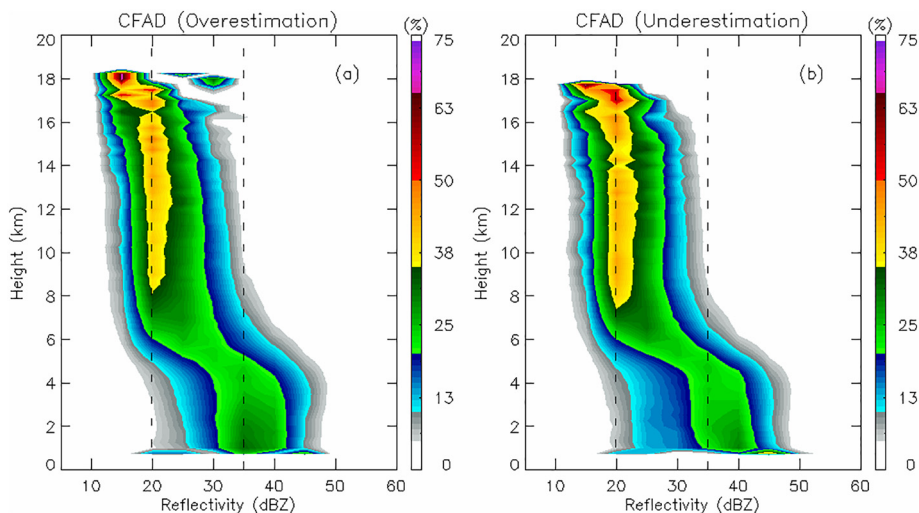


Fig. 4. Contour frequency by altitude diagrams (CFAD) of reflectivity according to height profile for overestimated and underestimated categories. The vertical lines indicate the reflectivities of 20 and 35 dBZ.

The CFADs are two-dimensional diagrams that provide the frequency, in this case, of reflectivity with height. In this way, it is possible to analyze the variability of the vertical profiles of reflectivity rather than the average value of the profile, which can sometimes mask the results. Fig. 4 presents the CFADs for the over- and under-estimated populations. The two CFADs are very similar, with only a few notable differences. The middle layer just above the melting layer shows the most important difference. The overestimated population shows higher reflectivity values at this level than the underestimated population. CFADs generated according to the precipitation intensity for the overestimated and underestimated populations (not shown) present more significant differences between populations. Fig. 3 shows proportionally higher rain rates for the overestimated population; therefore, we expect that the CFAD will also reproduce this feature. For a more detailed view of these two population features, the subsequent analysis focuses on properties of the cloud top and microphysical parameters.

To evaluate the echo-top height within each category, frequency distributions were generated according to the echo-top height. A threshold of 17 dBZ was used as the minimum detectable signal of the PR. Fig. 5 shows that the underestimated cases have larger relative populations with an echo-top height up to around 9 km, while overestimated cases have larger relative populations with echo tops above this height. This behavior is consistent with lower rain rates estimated by GPROF due to the lower ice water content of shallower clouds and the opposite in the case of deep convective clouds. However, both populations span the range of clouds tops, and the small differences in the CFADs cannot fully explain the retrieval errors. Another important consideration is the difference in the distribution of cloud tops as a function of the over- and under-estimation. The absolute error as a function of the cloud top and rain rate is showed in Fig. 5. Clearly, the overestimation does not depend on the cloud top, since the relative frequency of the cloud top remains almost constant despite changes in the error considered.

To explore biases in more details, the values of Liquid Water Path (LWP), and Ice Water Path (IWP), electrical discharges detected by LIS and the polarization difference at 85 GHz were also calculated.

The reflectivity profiles obtained from PR together with Eqs. 2 and 3 (Wang et al., 2007) were used to compute LWP and IWP. LWP was computed for the layer between the surface and the height of 5 km while IWP was calculated for the layer between 5 km and the cloud top.

$$LWP = 3.44 \times 10^{-3} \int_{surface}^{level0} [Z_H^{rain}]^{4/7} dH \quad (2)$$

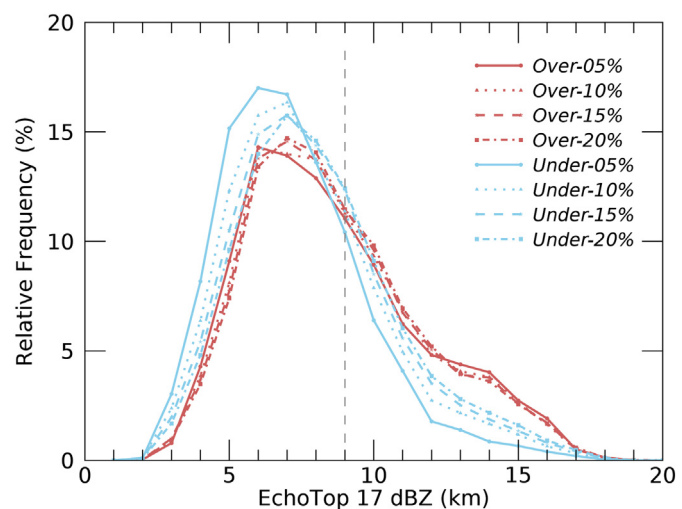


Fig. 5. Relative frequency distribution of echo-top 17 dBZ. Overestimated cases are indicated in red and underestimated cases in blue. Under- and over-estimated populations are classified by the 20%, 15%, 10% and 5% percentiles for the tail of the distribution. The vertical line indicates the height of 9 km. (For interpretation of the references to colour in this figure legend, the reader is referred to the web version of this article.)

$$IWP = 1000 \pi \rho_i N_0^{3/7} \int_{level0}^{htop} \left(\frac{5.28 \times 10^{-18} Z_H^{ice}}{720} \right)^{4/7} dH \quad (3)$$

where, Z_H^{rain} and Z_H^{ice} , in $\text{mm}^6 \text{m}^{-3}$, is the reflectivity below and above 5 km respectively, ρ_i is the density of ice (917 kg m^{-3}), N_0 ($4 \times 10^6 \text{ m}^{-4}$) is the intercept parameter, $level0$ is the altitude based on 0°C isotherm height (chosen as 5 km), $htop$ (km) is the cloud top and (km) is the altitude.

Fig. 6 shows histograms for the frequency distribution of IWP, flash rate (referred to as LIS), the 85 GHz polarization signal ($Tb_V - Tb_H$), the atmospheric scattering signal at 85 GHz (PCT85) and LWP. It was verified that, for the overestimated cases, there are relatively more cases with higher values of IWP and flash rates (Fig. 6a and b), more cases with 85 GHz polarization difference ($Tb_V - Tb_H$) < 2 K (Fig. 6c), and a slight difference for smaller values of LWP (Fig. 6e). For the underestimated cases, the exact opposite happens: slightly higher LWP values and lower IWP and LIS values, which is consistent with a lower PCT85 and an underestimation of the rain rate. The majority of underestimated

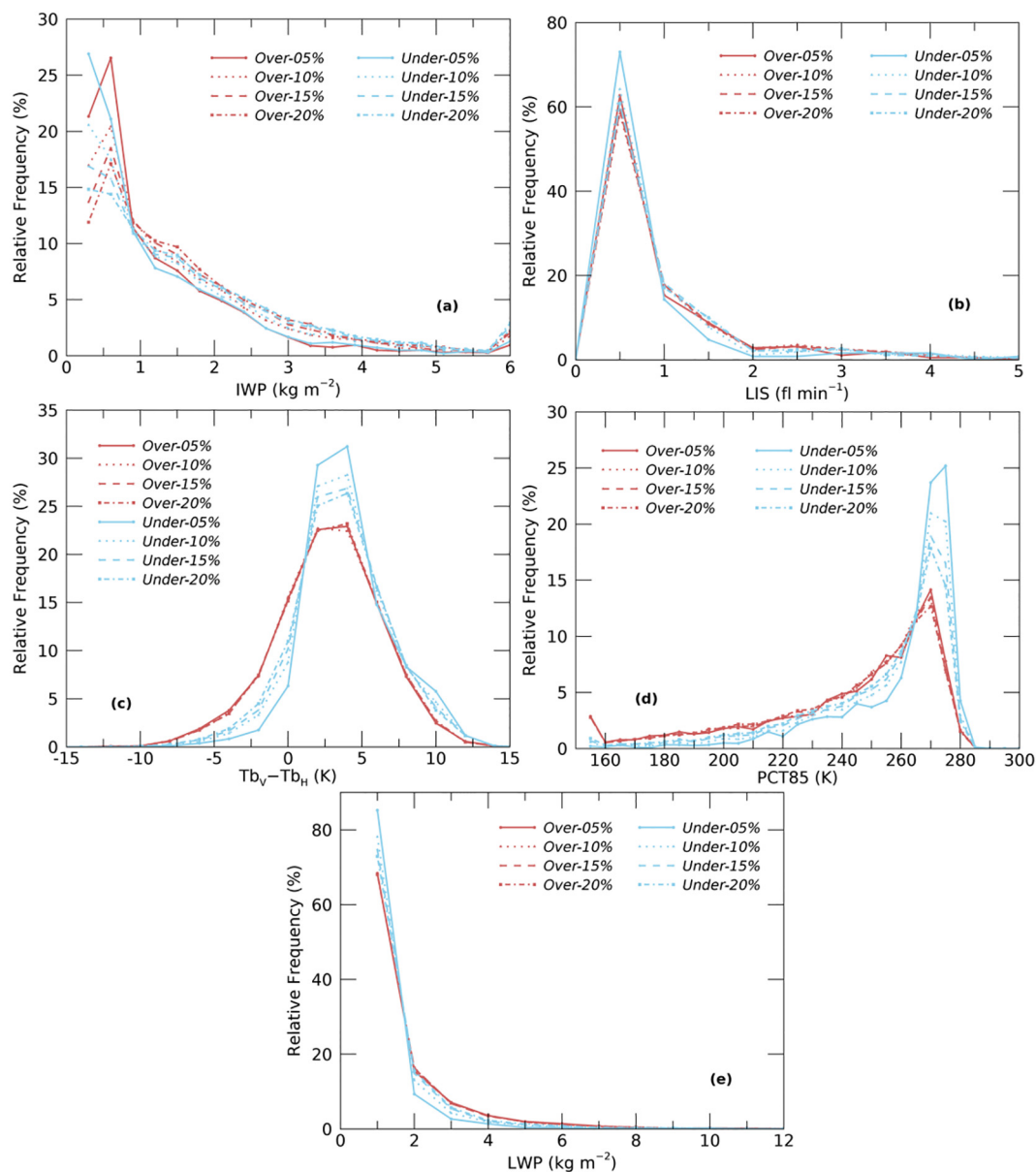


Fig. 6. Relative frequency distribution according: a) IWP; b) LIS; c) Polarization difference in T_b at 85 GHz; d) PCT at 85 GHz; and e) LWP. Overestimated cases are indicated in red and underestimated cases in blue. Under- and over-estimated are classified by the 20%, 15%, 10% and 5% percentiles for the tail of the distribution. (For interpretation of the references to colour in this figure legend, the reader is referred to the web version of this article.)

cases have positive polarization differences that are associated with frozen particles and stratiform cloud regions (Prigent et al., 2005). As expected the overestimated cases have a higher frequency of low PCT85, implying a large amount of scattering, while the opposite is observed for the underestimated cases where PCT85 occurrences peak at 270 K (Fig. 6d). For LWP, IWP and LIS, the differences between the categories are more subtle and less significant. It is important to note that for the flash rate frequency distributions over Amazon region (Fig. 6b), 96.6% of the underestimated cases and 94.7% of the overestimated cases do not have any lightning associated with them. Only 3.4% of the underestimated cases and 5.3% of the overestimated cases have flash rate higher than 0 flash min^{-1} . Wang et al. (2012) used the LIS data to understand the relationship between lightning flash rate and active and passive microwave precipitation observations. The study revealed that only 6% of the rain data have lightning flash rates greater than zero, nevertheless, 86.5% of lightning occurred over convective cloud and the remaining in stratiform clouds.

Fig. 6 also presents some interesting results related to the different

percentile populations used to define the outliers for all these parameters. PCT85, polarization, LWP and LIS have little variability across the different percentiles for the overestimation cases. Only for IWP there is a clear distinction among the different percentiles. The underestimated population absolute error is function of the rain rate, cloud top, LWP, IWP, PCT85 and polarization. As such, it is difficult to attribute the underestimation to any particular cause. However, the absolute error of the overestimated population is chiefly a function of the IWP. The result shown above illustrates some of the complexities in determining biases in passive microwave rain estimates.

An alternative analysis is therefore carried out that separates clouds by their maximum height, using 9 km to separate congestus and deeper convective cloud populations (see Wang et al., 2018). Petković and Kummerow (2017) also used the same cloud top classification. Composite reflectivity profiles for these two cloud top categories were stratified according to IWP for over- and under-estimated rain rates. Only cloud tops above 5 km were considered as this represents a cloud ice analysis. Fig. 7 presents the vertical reflectivity profiles of the over-

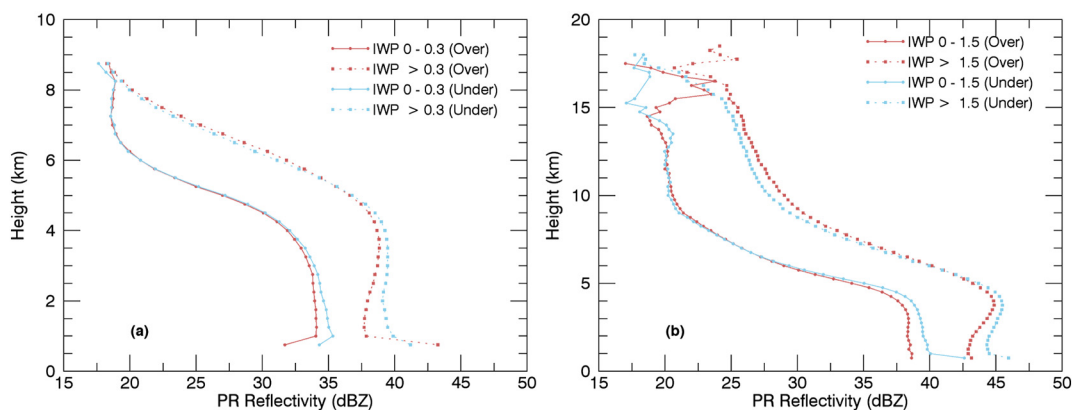


Fig. 7. Mean reflectivity profile of the underestimated and overestimated clouds populations for two classes of IWP values. a) Clouds with echo top below 9 km; b) Clouds with echo top above 9 km. Overestimated cases are indicated in red and underestimated cases in blue. (For interpretation of the references to colour in this figure legend, the reader is referred to the web version of this article.)

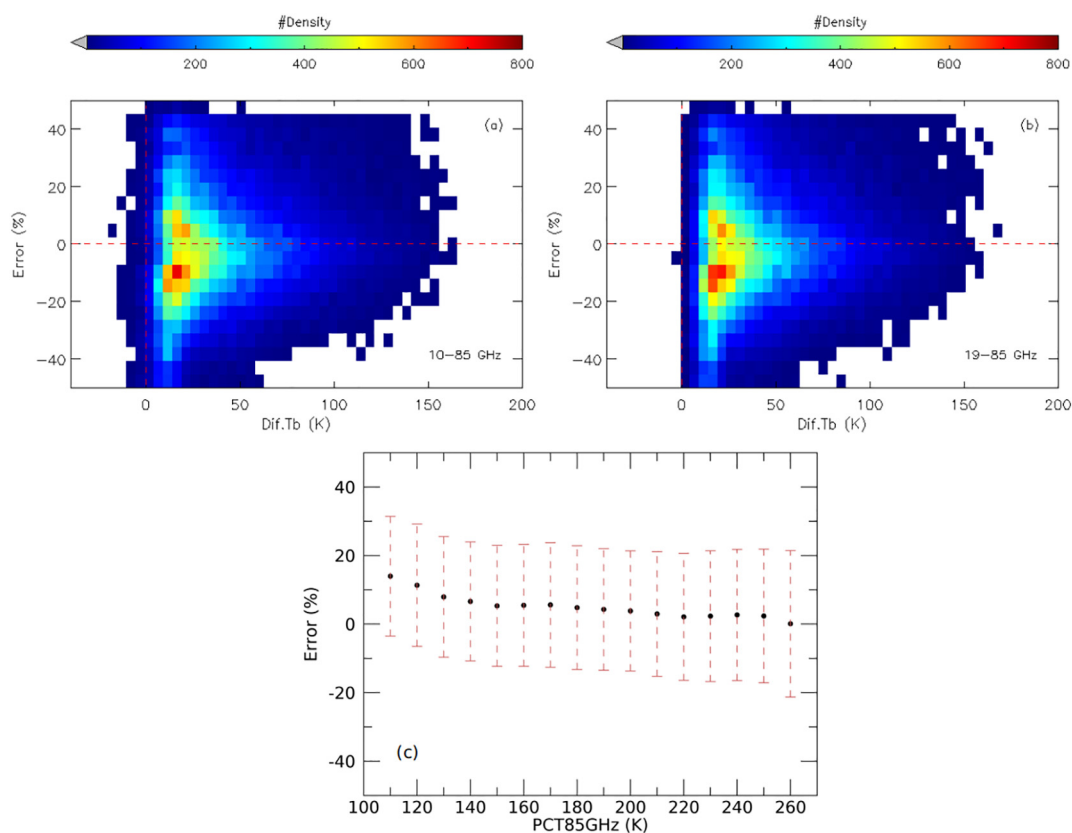


Fig. 8. Density scatter plot diagram for rainfall error estimation as function of the differences between the brightness temperatures a) 10–85 GHz; b) 19–85 GHz; and c) Bin 10 K mean value of the differences between rainfall error estimation as function of the PCT85.

and under-estimated populations for clouds above and below 9 km. The composites were classified as a function of the IWP, so one can expect similar profiles above 5 km. Below 5 km, however, overestimated and underestimated categories are very different. The underestimated category has higher reflectivity values below the melting layer than the overestimated cases. One physical process that could explain these lower reflectivity values found below the melting layer for overestimated cases is if the clouds are in the dissipation phase of their life cycle. In the dissipation phase, clouds normally have a considerable amount of ice associated to small rain rates. These underestimated cases are probably associated with efficient shallow warm cloud rainfall processes, but for deep convective clouds the same behavior is observed. One can note that the underestimated population of deep

convective clouds also shows smaller reflectivities above the melting layer for the higher IWP ($> 1.5 \text{ kg m}^{-2}$). These deep convective clouds have smaller amounts of ice and higher reflectivities in the lower levels. These are clouds with rainfall mainly originating from warm cloud processes with a reduced ice melting contribution to rain rate.

5. Multi channels approach to classify overestimation and underestimation cases

The previous sections detail the variability in PCT85 with respect to rain rate. Additional channels available on spaceborne radiometers, although usually associated with difficulty to interpret emissions signals, may help. Two filters using additional channels were developed to

better explain over- and under-estimated cases. The first one uses 10, 19 and 85 GHz channels, which corresponded better to the overestimated cases, while the second uses 10, 19, 21, 37 and 85 GHz channels, which corresponds better to the underestimation cases.

The behavior of the 85 GHz channel, which exhibits scattering from relatively small ice particles, is well known and studied by several authors (Gopalan et al., 2010; Wang et al., 2012). According to You et al. (2011) the combination of the 19 and 37 GHz or 21 and 37 GHz channels can explain ~10% more variance of near surface rainfall rate than can the Tb_v85 channel for most continental tropical regions. Exceptions are the desert, arid, and semi-arid areas, but these are not present in the current study area. The additional signal in the 19 and 37 GHz combination is due to liquid water information, which is more directly related to surface rainfall than ice water aloft. If two channels have similar emissivities, then their differences largely describe the liquid water absorption. In heavy rainfall conditions, the combination Tb_v19-Tb_v37, Tb_v37 and Tb_v85 are all correlated with near-surface rainfall. The highest correlations can be found at Tb_v37 or Tb_v21 channels, most likely because these clouds contain very large ice amounts that produce significant scatter even at these lower frequencies. To further explore the utility of additional channels, Fig. 8 shows the relationship among channel differences between 10 and 85 GHz (10–85 GHz) and 19–85 GHz, relative to the rainfall estimation errors. The density scatter plot of the TMI channels differences and PCT85 bins in 10 K bins are presented in Fig. 8a, b and c. Both differences show nearly the same behavior, with a very small population of negative differences and a reduction of the amplitude as positive differences increase. The negative differences correspond to the rare situation of less scattering at 85 GHz than the absorption at 10 GHz and 19 GHz. For the positive differences, there is no clear pattern aside from the error reduction as the differences increase. However, the number of overestimated cases increases as the brightness temperature differences increase. These are the situations with very high scattering at 85 GHz (high amount of ice) and less water in the liquid state, resulting in a lower absorption by the 10 GHz and 19 GHz channels. Fig. 8b shows the error and the 10 K bin mean PCT85. One can note that PCT85s colder than 180 K are statically associated with an overestimation in precipitation.

The idea of exploiting the absorption channels (10–37 GHz) was also pursued. Channel differences may have information if one assumes that their emissivity is relatively invariant over land. The difference would then represent an atmospheric signal that may be related to precipitation. Fig. 9 shows the density scatter plot between precipitation estimation errors against brightness temperature differences

between the channels 19–10 GHz, 21–10 GHz and 37–21 GHz for all cases classified as convective. The differences between the brightness temperatures basically vary between –60 and 40 K and there is no clear pattern among the difference and the error. This lack of signal between these closely spaced frequencies does not allow these frequencies to be used to reduce rainfall estimation error.

6. Conclusions

This study evaluates the rainfall estimation error from a well known passive microwave algorithm. The error was defined as the absolute error between the rainfall estimated by GPROF and the TRMM PR. The error categories were defined in the range of percentiles: 0% to 5%, 10%, 15% and 20% for the tail of the distribution.

This allowed us to examine the relationship between the rainfall bias and a number of different variables (IWP, lightning, polarization, LWP, PCT85, cloud top heights and reflectivity vertical profiles). These analyses were done with the goal of classifying and understanding the cloud characteristics that lead to errors in the passive microwave estimation.

The population of underestimated rainfall cases can be associated with lower rain rates than overestimated cases. It implies that the absolute error for underestimated cases comes predominantly from rain rates < 2.5 mm h⁻¹. Overestimated cases, in contrast, tend to have larger rain rates. Moreover, the degree of bias tends to be correlated with the rain rates for underestimation, while the overestimation errors are uncorrelated with the rain rate itself.

The vertical profile of reflectivities, the CFADs, did not show large differences among the over- and under-estimated cases. As the CFAD also depends on the rain rate, and the overestimated population is associated with larger rain rate, the differences between the two populations may be difficult to interpret. Therefore, the analysis was made as function of the microphysical parameters and classes of IWP.

The echo top analysis showed larger populations of cumuliform clouds in the underestimated population when compared to the overestimated population that is more consistent with deep convective clouds (> 9 km). The underestimated cloud top distributions change as function of the error, with larger errors associated with lower cloud tops. This corresponds physically to warm rainfall processes which have significantly less ice. This lack of ice, in turn, causes the passive microwave retrievals that rely on ice scattering to severely underestimate the rainfall. In contrast, the overestimated population is not a function of the echo top. The relative amount of bias that is, does not appear to change with the cloud top distribution.

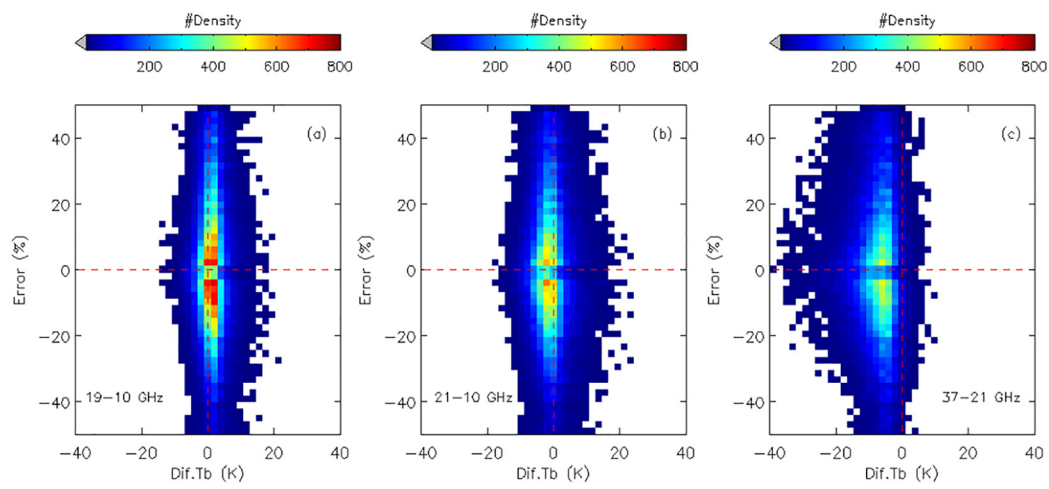


Fig. 9. Density scatter plot of differences between the estimated precipitation rate from the TMI and PR and the differences between the brightness temperatures: a) 19–10 GHz; b) 21–10 GHz; and c) 37–21 GHz for all convective cases.

The polarization signature shows the greatest contrast between the over- and under-estimated cases. The underestimated population is more prone to have positive values that are often associated with horizontally oriented particles such as snow in stratiform precipitation. The overestimated population, in contrast, exhibits polarization differences close to zero. This is generally associated with the deep convective regions with semi-spherical graupel or hail particles. Overestimation errors do not appear to be a function of the polarization difference.

Warmer values of PCT85 are common in the underestimated population, in agreement with lower cloud tops and warm rain processes. The overestimated population is associated with colder PCT85 but the error is not a function of the PCT85 value. LWP diagnostics also showed results similar to other findings. The underestimated population is dominated by smaller values ($LWP < 2 \text{ kg m}^{-2}$) with the error correlated to the LWP itself. Flash rates, which represent only few percent of the cases in both populations, also show similar trends. The underestimated population has fewer flashes than the overestimated population, as expected. The IWP distributions showed that the underestimated population has smaller values of IWP while the overestimated cases have larger values of IWP. In this case, however, the bias was seen to depend on the IWP itself. This feature clearly shows that overestimation errors are associated with the excess ice aloft. There is no relationship in the overestimated cases with cloud top height, PCT85, LWP or polarization. We speculate here that the ice excess could be related to cloud life cycle issues when clouds have large amounts of ice but small rain rates.

The reflectivity vertical profiles for under- and over-estimated cases analyzed as a function of IWP classes and cloud top populations ($< 9 \text{ km}$ vs $> 9 \text{ km}$) presented interesting results. The underestimated cases have larger reflectivities values in lower levels than their overestimated counterparts, while the overestimated population of deep convective clouds have higher reflectivity in the upper levels and smaller reflectivities in the lower levels.

The final analysis examined whether additional channels in addition to the scattering channels were useful predictors of the overall biases. The radiance measured by the microwave sensors is a combination of surface and cloud-atmosphere emission/scattering. Channel differences can eliminate the surface emission if surface emissivities are similar. Therefore, channel differences with 85 GHz and between more similar wavelengths were tested to check their effectiveness in reproducing observed bias structures. Results suggested that the error is reduced as the positive differences between 10 and 19 GHz channels and ice scattering channel (i.e. 85 GHz) increase. Using channels difference among neighboring channels showed very little correlation with the observed rainfall biases.

The results presented in this study show a fairly robust statistical relationship between the ice in cloud structures and the bias from passive microwave sensors over the Amazon. This knowledge can help to establish adjustments to improve rainfall estimation over tropical land regions.

Acknowledgments

This research was supported by SOS CHUVA FAPESP project 2015/14497-0. The authors acknowledge the University of Utah for providing the TRMM data.

References

- Awaka, J., Toshio, I., Ken'ichi, O., 2009. TRMM PR standard algorithm 2A23 and its performance on bright band detection. *J. Meteorol. Soc. Jpn.* 87, 31–52. <http://dx.doi.org/10.2151/jmsj.87A.31>.
- Carr, N., Kirstetter, P., Hong, Y., Gourley, J.J., Schwaller, M., Petersen, W., Wang, N., Ferraro, R.R., Xue, X., 2015. The influence of surface and precipitation characteristics on TRMM microwave imager rainfall retrieval uncertainty. *J. Hydrometeorol.* 16, 1596–1614. <http://dx.doi.org/10.1175/JHM-D-14-0194.1>.
- Ferraro, R.R., Weng, F., Grody, N., Zhao, L., Meng, H., Kongoli, C., Pellegrino, P., Qiu, S., Dean, C., 2005. NOAA operational hydrological products derived from the advanced microwave sounding unit. *IEEE Trans. Geosci. Remote Sens.* 43, 1036–1049.
- Giangrande, S.E., Feng, Z., Jensen, M.P., Comstock, J.M., Johnson, K.L., Toto, T., Wang, M., Burleyson, C., Bharadwaj, N., Mei, F., Machado, L.A.T., Manzi, A.O., Xie, S., Tang, S., Silva Dias, M.A.F., de Souza, R.A.F., Schumacher, C., Martin, S.T., 2017. Cloud characteristics, thermodynamic controls and radiative impacts during the Observations and Modeling of the Green Ocean Amazon (GoAmazon2014/5) experiment. *Atmos. Chem. Phys.* 17, 14519–14541. <http://dx.doi.org/10.5194/acp-17-14519-2017>.
- Gopalan, K., Wang, N., Ferraro, R., Liu, C., 2010. Status of the TRMM 2A12 land precipitation algorithm. *J. Atmos. Ocean. Technol.* 27, 1343–1354. <http://dx.doi.org/10.1175/2010JTECHA1454.1>.
- Iguchi, T., Kozu, T., Meneghini, R., Awaka, J., Okamoto, K., 2000. Rain-profiling algorithm for the TRMM precipitation radar. *J. Appl. Meteorol.* 39, 2038–2052. [http://dx.doi.org/10.1175/1520-0450\(2001\)040<2038:RPAFTT>2.0.CO;2](http://dx.doi.org/10.1175/1520-0450(2001)040<2038:RPAFTT>2.0.CO;2).
- Kidd, C., Levizzani, V., 2011. Status of satellite precipitation retrievals. *Hydrol. Earth Syst. Sci.* 15, 1109.
- Kidd, C., Tan, J., Kirstetter, P.-E., Petersen, W.A., 2017. Validation of the Version 05 Level 2 precipitation products from the GPM Core Observatory and constellation satellite sensors. *Q.J.R. Meteorol. Soc.* <https://doi.org/10.1002/qj.3175>.
- Kummerow, C., Olson, W.S., Giglio, L., 1996. A simplified scheme for obtaining precipitation and vertical hydrometeor profiles from passive microwave sensors. *IEEE Trans. Geosci. Remote Sens.* 34, 1213–1232.
- Kummerow, C., Hong, Y., Olson, W.S., Yang, S., Adler, R.F., McCollum, J., Ferraro, R., Petty, G., Shin, D.-B., Wilhelm, T.T., 2001. The evolution of the Goddard profiling algorithm (GPROF) for rainfall estimation from passive microwave sensors. *J. Appl. Meteorol.* 40, 1801–1820. <https://doi.org/10.1175/1520-0450>.
- Kummerow, C.D., Ringerud, S., Crook, J., Randel, D., Berg, W., 2011. An observationally generated a priori database for microwave rainfall retrievals. *J. Atmos. Ocean. Technol.* 28, 113–130. <http://dx.doi.org/10.1175/2010JTECHA1468.1>.
- Liu, C., 2013. University Utah TRMM precipitation and cloud feature database, Description Version 2.0. http://atmos.tamucc.edu/trmm/data/document/TRMM_database_description_2.0_201308.pdf.
- Mattos, E.V., Machado, L.A.T., 2011. Cloud-to-ground lightning and mesoscale convective systems. *Atmos. Res.* 99, 377–390. <http://dx.doi.org/10.1016/j.atmosres.2010.11.007>.
- Nesbitt, S.W., Zipser, E.J., Cecil, D.J., 2000. A census of precipitation features in the tropics using TRMM: radar, ice scattering, and lightning observations. *J. Clim.* 13, 4087–4106. [http://dx.doi.org/10.1175/1520-0442\(2000\)013<4087:ACOPFI>2.0.CO;2](http://dx.doi.org/10.1175/1520-0442(2000)013<4087:ACOPFI>2.0.CO;2).
- Petersen, W.A., Hugh, J.C., Steven, A.R., 2005. TRMM observations of the global relationship between ice water content and lightning. *Geophys. Res. Lett.* 32, L14819. <https://doi.org/10.1029/2005GL023>.
- Petković, V., Kummerow, C.D., 2017. Understanding the sources of satellite passive microwave rainfall retrieval systematic errors over land. *J. Appl. Meteorol. Climatol.* 56, 597–614. <http://dx.doi.org/10.1175/JAMC-D-16-0174.1>.
- Prigent, C., Defer, E., Pardo, J.R., Pearl, C., Rossow, W.B., Pinty, J.-P., 2005. Relations of polarized scattering signatures observed by the TRMM microwave instrument with electrical processes in cloud systems. *Geophys. Res. Lett.* 32, L04810. <https://doi.org/10.1029/2004GL022225>.
- Rozante, J.R., Moreira, D.S., de Goncalves, L.G.G., Vila, D.A., 2010. Combining TRMM and surface observations of precipitation: technique and validation over South America. *Weather Forecast.* 25, 885–894. <http://dx.doi.org/10.1175/2010WAF2222325.1>.
- Silva Dias, M.A.F., Cohen, J.C.P., Gandú, A.W., 2005. Interações entre nuvens, chuvas e a biosfera na Amazônia. *Acta Amazon.* 35, 215–222. <https://doi.org/10.1590/S0044-59672005000200011>.
- Spencer, R.W., Goodman, H.M., Hood, R.E., 1989. Precipitation retrieval over land and ocean with the SSM/I: identification and characteristics of the scattering signal. *J. Atmos. Ocean. Technol.* 6, 254–273. [https://doi.org/10.1175/1520-0426\(1989\)006b0254:PROLAON2.0.CO;2](https://doi.org/10.1175/1520-0426(1989)006b0254:PROLAON2.0.CO;2).
- Vila, D., Ferraro, R., Joyce, R., 2007. Evaluation and improvement of AMSU precipitation retrievals. *J. Geophys. Res. Atmos.* 112, D20119. <https://doi.org/10.1029/2007JD008617>.
- Wang, J., Li, X., L., Carey, L.D., 2007. Evolution, structure, cloud microphysical, and surface rainfall processes of monsoon convection during the South China Sea monsoon experiment. *J. Atmos. Sci.* 64, 360–380. <https://doi.org/10.1175/JAS3852.1>.
- Wang, N.-Y., Gopalan, K., Albrecht, R.I., 2012. Application of lightning to passive microwave convective and stratiform partitioning in passive microwave rainfall retrieval algorithm over land from TRMM. *J. Geophys. Res.* 117, D23203. <https://doi.org/10.1029/2012JD017812>.
- Wang, D., Giangrande, S.E., Bartholomew, M.J., Hardin, J., Feng, Z., Thalman, R., Machado, L.A., 2018. The Green Ocean: precipitation insights from the GoAmazon2014/5 experiment. *Atmos. Chem. Phys. Discuss.* <http://dx.doi.org/10.5194/acp-2018-101>. (in review).
- Weng, F., Zhao, L., Ferraro, R.R., Poe, G., Li, X., Grody, N.C., 2003. Advanced microwave sounding unit cloud and precipitation algorithms. *Radio Sci.* 38, 8068. <http://dx.doi.org/10.1029/2002RS002679>.
- You, Y., Liu, G., Wang, Y., Cao, J., 2011. On the sensitivity of tropical rainfall measuring mission (TRMM) microwave imager channels to overland rainfall. *J. Geophys. Res. Atmos.* 116, D12203. <http://dx.doi.org/10.1029/2010JD015345>.